CHAPTER VI

EFFECT OF CATALYST PREPARATION ON $Au/Ce_{1-x}Zr_xO_2$ AND $Au–Cu/Ce_{1-x}Zr_xO_2$ FOR STEAM REFORMING OF METHANOL*

6.1 Abstract

We tested 3 wt% gold (Au) catalysts on CeO_2–ZrO_2 mixed oxides, prepared by coprecipitation (CP) and the sol-gel (SG) technique, for steam reforming of methanol (SRM). Uniform $Ce_{1-x}Zr_xO_2$ solid solution was dependent on the Zr/Ce ratio, where the incorporation of Zr^{4+} into the Ce^{4+} lattice with a ratio of 0.25 resulted in smaller ceria crystallites and better reducibility, and was found to be efficient for SRM activity. The catalytic activity was suppressed when the ratio was ≥ 0.5, which led to the segregation of Zr from solid solution and sintering of Au nanoparticles. It was found that the CP technique produced better catalysts than SG in this case. For the bimetallic catalysts, the co-operation of Au–Cu supported on $Ce_{0.75}Zr_{0.25}O_2$ (CP) exhibited superior activities with complete methanol conversion and low CO concentration at 350 °C. Furthermore, the size of the alloy particle was strongly dependent on the pH level during preparation.

Keywords: Steam Reforming of Methanol; Hydrogen; Alloy; Solid solution; CeO_2; ZrO_2

6.2 Introduction

In recent years, there have been an intensive research efforts to find new technologies which are more environmentally friendly than the internal combustion engines in terms of their green house emissions [1,2]. Among the viable solutions, the use of a proton exchange membrane fuel cell (PEMFC) is an attractive technology that has high-energy conversion efficiency to generate electricity for automotive applications [3,4]. The ideal reactant for PEMFC is hydrogen (H_2); however, the hydrogen produced by on-board reforming should not contain more than 10 ppm CO to protect the Pt electrode in the PEMFC [5]. Among H_2 production

* International Journal of Hydrogen Energy, 38 (2013) 1348–1362.

processes, steam reforming of methanol (SRM) is promising, compared to the use of hydrocarbons [6,7] and other oxygenated reactants [8], as shown in Eq (6.1).

$$CH_3OH + H_2O \rightarrow CO_2 + 3H_2 \qquad \Delta H(298\ K) = 50\ kJ\ mol^{-1} \qquad (6.1)$$

However, this reaction still contains CO as a by-product via methanol decomposition (DM) [5]. The selection of the specific catalysts is important to promote SRM and reduce CO altogether. Copper-based catalysts [9,10] were investigated for SRM due to their high activity. Unfortunately, Cu-based catalysts rapidly deactivate due to pyrophoric deposits forming on its surface at high temperatures (> 270 °C) [11]. In contrast, there are publications reporting positive aspects of Au-based catalysts for this reaction [5,12]. Au-based catalysts are also highly active catalysts for preferential CO oxidation (PROX) [13] and water-gas shift (WGS) reactions [14], resulting in minute amounts of CO in the products. However, Au catalyst activity depends strongly on Au dispersion, particle size, and number of interaction sites [12]. As a support, ceria (CeO_2) has high oxygen storage capacity (OSC) or oxygen vacancy, to store and release active oxygen during the reaction [15]. Moreover, the incorporation of some cations, $M^{\delta+}$ (M = Fe, Zr, Si, etc), into the Ce^{4+} lattice, results in increased vacancy sites in the anion sublattice which results in better redox properties [16,17]. According to our previous study in 2012 [18], the Au/CeO_2–Fe_2O_3 catalysts exhibited 100% methanol conversion and 74% H_2 yield at 300 °C in the SRM. The high activity was attributed to the formation of a $Ce_xFe_{1-x}O_2$ solid solution [18], but it rapidly deactivated under reaction conditions. There are reports [19,20] of incorporation of zirconia into the ceria lattice to prevent sintering of ceria crystallites, to preserve the oxygen vacancies, and suppress CO formation, which is believed to be the source of coke deposition [8]. As mentioned previously, the CeO_2–ZrO_2 support seems to be a promising material to obtain high SRM activity with low CO levels (< 10 ppm). Our goal is to achieve significant improvement with low temperature activity (200–300 °C) of the Au catalyst. It is preferable to produce as high purity H_2 in SRM as possible at low temperatures ($T \leq 300$ °C) before sending the product streams to the PROX unit for reduction of the CO to the desirable limits. A second goal is to use as low of a Au loading as possible, because

of its cost, by adding a cheaper metal (such as Cu) to improve upon the pure gold catalysts.

Earlier studies have shown that the co-addition of Cu and Au at low loadings (1–2 wt% total loading) prevented sintering of Au and provided the Au–Cu alloy in partial oxidation of methanol [21,22]. Many parameters were optimized for the Au–Cu catalysts, such as pH value during catalyst preparation, Au/Cu atomic ratio, and calcination temperature [22]. Pongstabodee et al. studied the activity of 5 wt% Au/CuO–CeO_2 catalyst in SRM and found that the role of additional CuO was to promote CuO reduction by interacting with Au, to form a solid solution inside the CeO_2 lattice, resulting in high methanol conversion [23]. Therefore, it would be beneficial to exploit the advantages of both Au–Cu alloy (active metal) and $Ce_xZr_{1-x}O_2$ solid solution (active support) to provide superior catalytic activity in SRM. Based on our knowledge, the Au–Cu bimetallic catalyst has not been used for SRM before.

In this study, the activity of Au/CeO_2–ZrO_2 and Au–Cu/CeO_2–ZrO_2 catalysts, prepared by the deposition technique, were investigated in SRM (200–500 °C) in terms of H_2 production and CO concentration.

6.3 Experimental

6.3.1 Catalyst preparation

The CeO_2–ZrO_2 mixed oxide supports were first prepared by the co-precipitation (CP) and sol-gel (SG) methods, while the pure CeO_2 and ZrO_2 supports were prepared by the precipitation method. All supports were designed to obtain $Ce_{1-x}Zr_xO_2$ solid solution, where x was the atomic ratio of Zr/(Ce + Zr), and was varied at 0, 0.25, 0.50, 0.75, and 1.0.

6.3.1.1 Co-precipitation (CP) method

Appropriate amounts of 0.1 M aqueous solutions—cerium (III) nitrate hexahydrate ($Ce(NO_3)_3.6H_2O$; Aldrich), zirconium (IV) oxide chloride octahydrate ($ZrOCl_2.8H_2O$; Merck), and Na_2CO_3 (Riedel-de Haen)—were mixed under vigorous stirring conditions at 80 °C and pH 8. Afterwards, the precipitate was

washed with warm deionized water to eliminate residual ions. The deionized precipitate was dried at 110 °C and calcined in air at 400 °C for 4 h in order to obtain CeO_2–ZrO_2 supports.

6.3.1.2 Sol-gel (SG) method

Each 0.1 M of two metal salt solutions—$Ce(NO_3)_3.6H_2O$ and $ZrOCl_2.8H_2O$—were mixed with 0.4 M of urea solution at a 2 to 1 volumetric ratio. The ratio between each metal salt was altered depending on the desired solid solution composition. Each solution was kept at 100 °C for 50 h. The samples were then allowed to cool to room temperature before being centrifuged to separate the solid product from the solution. The solid product was washed with ethanol to prevent an agglomeration of particles, then dried, followed by calcination in air at 400 °C for 4 h [24].

In the Au deposition experiment, the total metal loading was fixed at 3 wt%. An aqueous solution of $HAuCl_4.3H_2O$ (Alfa AESAR) was heated to 80 °C and the pH was adjusted to pH 8 by the addition of Na_2CO_3. The resulting solution was stirred for 1 h, then washed, dried, and calcined in air at 400 °C for 4 h. For the Cu deposition experiment, the preparation technique was similar to Au deposition, where the metal aqueous solution was copper(II) nitrate trihydrate ($Cu(NO_3)_2.3H_2O$; MERCK).

For preparing the bimetallic Au–Cu/$Ce_{1-x}Zr_xO_2$ (1.5 wt% Au and 1.5 wt% Cu), two metal aqueous solutions—$Cu(NO_3)_2.3H_2O$ and $HAuCl_4.3H_2O$—were mixed and then heated to 80 °C while varying the pH from 6 to 9 by adding Na_2CO_3. The resulting solution was stirred for 1 h, then the suspension was washed, dried, and calcined in air for 4 h at 400 °C.

6.3.2 Catalyst characterization

Powder XRD measurements were carried out on a JEOL X-Ray diffractometer system (JDX-3530) with a CuK_α (1.5406 Å) X-ray source operating at 40 kV and 30 mA.

The size and distribution of the Au particles deposited on the supports were directly observed by a JEOL, JEM 2010 transmission electron microscope (TEM) at an accelerating voltage of 200 kV in bright field mode. Before being transferred into the TEM chamber, the samples were dispersed in ethanol and then dropped onto a copper grid. The volume-area average Au particle size diameter (d_{TEM}) was calculated from the following formula: $d_{TEM} = \Sigma(n_i d_i^3)/(n_i d_i^2)$, where n_i is the number of Au particles of diameter d_i.

UV-vis spectroscopy experiments checked for the presence of different states of oxidation of the contained metal. The measurements were performed on air-exposed samples at ambient temperature between 200 and 800 nm with a Shimadzu 2550 UV spectrometer. The absorption intensity was expressed using the Kubelka-Munk function, $F(R\infty) = (1-R\infty)^2/(2R\infty)$, where $R\infty$ is the diffuse reflectance from a semi-infinite layer.

An X-Ray Fluorescence Spectrometer, XRF (AXIOS PW4400), was used to determine the actual surface (Au, Cu, Ce, and Zr) composition.

Temperature-programmed reduction (TPR) of the catalysts was carried out in a conventional TPR reactor with a 30 ml/min of 10% H_2 in argon with a conventional TPR reactor equipped with a thermal conductivity detector. The reduction temperature was raised from 30 to 850 °C at a ramp rate of 10 °C/min.

6.3.3 Catalytic activity measurements

The SRM reaction was carried out in a fixed-bed reactor containing 100 mg of catalyst under atmospheric pressure from 200 to 500 °C. A mixture of distilled water and methanol was injected continuously by a syringe pump at a rate of 1.5 mL h^{-1} to a vaporizer, which was mixed with He carrier gas before entering the catalytic reactor. The H_2O/CH_3OH molar ratio was fixed at 2/1. The gas hourly space velocity (GHSV) was kept at 21 000 mL/g-cat. h. The product gases (e.g. H_2, CO, CO_2, and CH_4) from the reactor were analyzed both by auto-sampling in an on-line gas chromatograph, Agilent 6890N, with a packed carbosphere (80/100 mesh) column (10 ft x 1/8 inch), and a thermal conductivity detector (TCD). The selectivity

of each product gas was defined by the mole percentage in the product stream. No methane formation was observed in this study.

6.4 Results and discussion

6.4.1 Catalyst characterization

The chemical and physical properties of the series of $Au/CeO_2–ZrO_2$ catalysts are summarized in Table 6.1. For the $CeO_2–ZrO_2$ supports, all Ce and Zr concentrations, designated as the x values, were close to the expected values for both CP and SG techniques, suggesting that the mixed oxide supports could be synthesized correctly with these techniques. In terms of actual Au loading, the CP samples gave more accurate results than the SG samples, implying that the amounts of Au deposited on the SG supports were difficult to be precisely controlled under the preparation conditions. It was noted that the variation in Ce/Zr ratio displayed different chemical properties in both support types (i.e. Au-support interaction site and/or point of zero charge (PZC) values), resulting in the deviation in percentage of Au loading [25,26]. For both supports, the amounts of Au deposited decreased with increasing Zr content since the PZC of the oxide support significantly affected the interaction of the Au precursor during the deposition step. In the deposition process at a solution pH of 8, the Au precursor was in the form of $[AuCl(OH)_3]^-$ and $[Au(OH)_4]^-$ [27,28], which were negatively charged. According to PZC value, the pure CeO_2 and ZrO_2 was measured at approximately 7.27 and 4.87, respectively, while the $Ce_{0.75}Zr_{0.25}O_2$, $Ce_{0.5}Zr_{0.5}O_2$, and $Ce_{0.25}Zr_{0.75}O_2$ (CP/SG) supports were detected at 7.20/4.96, 6.97/4.64, and 5.69/4.05, respectively. However, the PZC values of the CeO_2 and ZrO_2 supports were different from those observed in previous literature [29,30]. As expected, the results showed the same trends; the PZC decreased with increasing Zr contents for both SG and CP supports. It is well known that the charge on the mixed oxide support strongly depends on the PZC and the pH level. If the pH of the solution is lower than the PZC of the support, the surface charge will be positive due to the protonation of the surface hydroxyls, so higher Au anion uptake is possible due to an electrostatic adsorption force [22]. If the pH of the solution is higher than the PZC of the support, the surface charge will be negative

due to the removal of protons from the surface hydroxyls, resulting in an electrostatic repulsion force of Au anions. Even though all synthesized supports had PZC values lower than the pH solution (~8) in this case, the different value between the pH and PZC was still useful for briefly approximating the amount of charge on the surface. The lower PZC the support had, the more negatively charged the surface became. Consequently, the surface of the rich Zr samples ($Ce_{0.5}Zr_{0.5}O_2$ and $Ce_{0.25}Zr_{0.75}O_2$) has more negative charges than the rich Ce sample ($Ce_{0.75}Zr_{0.25}O_2$) resulting in greater removal of protons from the surface hydroxyls and stronger electrostatic repulsion of Au anions, which caused difficulty in Au deposition. This was the reason why the amount of Au deposited decreased in the Zr rich samples. In comparison with the preparation routes for the CeO_2–ZrO_2 support, the SG samples had much lower PZC values than those of CP samples at the same Ce/Zr ratio. Thus, the charge on the SG support surface became more negative, and then resulted in much stronger electrostatic repulsion of Au anions. To better understand the above statements, a schematic drawing of the changes in the mixed oxide supports with various support compositions is shown in Fig. 6.1A.

Table 6.1 Chemical-physical properties of the monometallic $Au/Ce_{1-x}Zr_xO_2$ catalysts

Catalysts[a]	Au* (wt%)	Ce* (wt%)	Zr* (wt%)	Crystallite size[b] (nm)	Expected x value**	Synthesized x value**	Lattice constant of CeO_2[c] (nm)	Au crystallite size (nm) d_{111}	d_{200}	d_{220}
3 wt% Au/CeO_2	2.74	97.26	-	7.65	0.00	0.00	0.544	< 5	-	-
3 wt% $Au/Ce_{0.75}Zr_{0.25}O_2$ (CP)	2.92	81.18	15.90	7.21	0.25	0.23	0.539	7.78	-	-
3 wt% $Au/Ce_{0.5}Zr_{0.5}O_2$ (CP)	2.61	66.48	30.92	4.69	0.50	0.42	0.532	12.12	-	-
3 wt% $Au/Ce_{0.25}Zr_{0.75}O_2$ (CP)	2.68	30.90	66.42	5.95	0.75	0.77	0.535	23.84	20.16	-
3 wt% $Au/Ce_{0.75}Zr_{0.25}O_2$ (SG)	2.33	81.93	15.74	8.73	0.25	0.23	0.543	15.35	-	-
3 wt% $Au/Ce_{0.5}Zr_{0.5}O_2$ (SG)	1.98	59.80	38.22	8.64	0.50	0.50	0.540	20.41	15.36	29.56
3 wt% $Au/Ce_{0.25}Zr_{0.75}O_2$ (SG)	1.85	40.62	57.53	9.79	0.75	0.69	0.542	23.58	21.51	24.06
3 wt% Au/ZrO_2	2.15	-	97.85	-	1.00	1.00	-	8.99	7.12	22.93

*The percentage of each metal was measured quantitatively by XRF.

**The "x" value was defined as the Zr/(Ce + Zr) mole ratio, which was calculated from $\frac{\frac{wt\%\ Zr}{MW\ of\ Zr}}{\frac{wt\%\ Zr}{MW\ of\ Zr}+\frac{wt\%\ Ce}{MW\ of\ Ce}}$ (Molecular weight of Zr metal = 91.22 g/mole and Molecular weight of Ce metal = 140.1 g/mole).

[a]All of samples were adjusted to pH 8 and calcined at 400 °C.

[b]Mean crystallite sizes were calculated from the average values of CeO_2 plane (111), (220), and (311).

[c]Unit cell parameter calculated from CeO_2 (220) with Bragg's equation.

Table 6.2 Chemical-physical properties of the bimetallic Au–Cu/$Ce_{0.75}Zr_{0.25}O_2$ catalysts

Catalysts[a]	pH	Au* (wt%)	Cu* (wt%)	Ce* (wt%)	Zr* (wt%)	Expected Au/Cu ratio**	Synthesized Au/Cu ratio**	Crystallite size (nm) CeO_2[b]	Crystallite size (nm) Au (111)	Lattice constant[c] (nm) CeO_2	Lattice constant[c] (nm) Au
1.5 wt% Au and 1.5 wt% Cu/$Ce_{0.75}Zr_{0.25}O_2$	6	1.31	1.21	82.72	14.77	0.33	0.35	9.37	15.06	0.540	0.4063
1.5 wt% Au and 1.5 wt% Cu/$Ce_{0.75}Zr_{0.25}O_2$	7	1.47	1.37	82.63	14.53	0.33	0.35	7.26	14.81	0.540	0.4050
1.5 wt% Au and 1.5 wt% Cu/$Ce_{0.75}Zr_{0.25}O_2$	8	1.32	1.24	81.05	16.39	0.33	0.34	8.02	16.66	0.540	0.4063
1.5 wt% Au and 1.5 wt% Cu/$Ce_{0.75}Zr_{0.25}O_2$	9	1.24	1.19	83.52	14.04	0.33	0.34	8.33	13.11	0.540	0.4076
3 wt% Cu/$Ce_{0.75}Zr_{0.25}O_2$	7	0.00	5.18	83.24	11.58	-	-	8.35	-	0.540	-

*The percentage of each metal was measured quantitatively by XRF.

**The Au/Cu atomic ratio was calculated from $\frac{wt\%\ Au}{MW\ of\ Au} \div \frac{wt\%\ Cu}{MW\ of\ Cu}$, where the molecular weight of Au metal is 196.967 g/mole and the molecular weight of Cu metal is 63.546 g/mole).

[a]All of samples were calcined at 400 °C.

[b]Mean crystallite sizes were calculated from the average values of CeO_2 plane (111), (220), and (311).

[c]Unit cell parameters calculated from CeO_2 (220) and Au (111) with Bragg's equation.

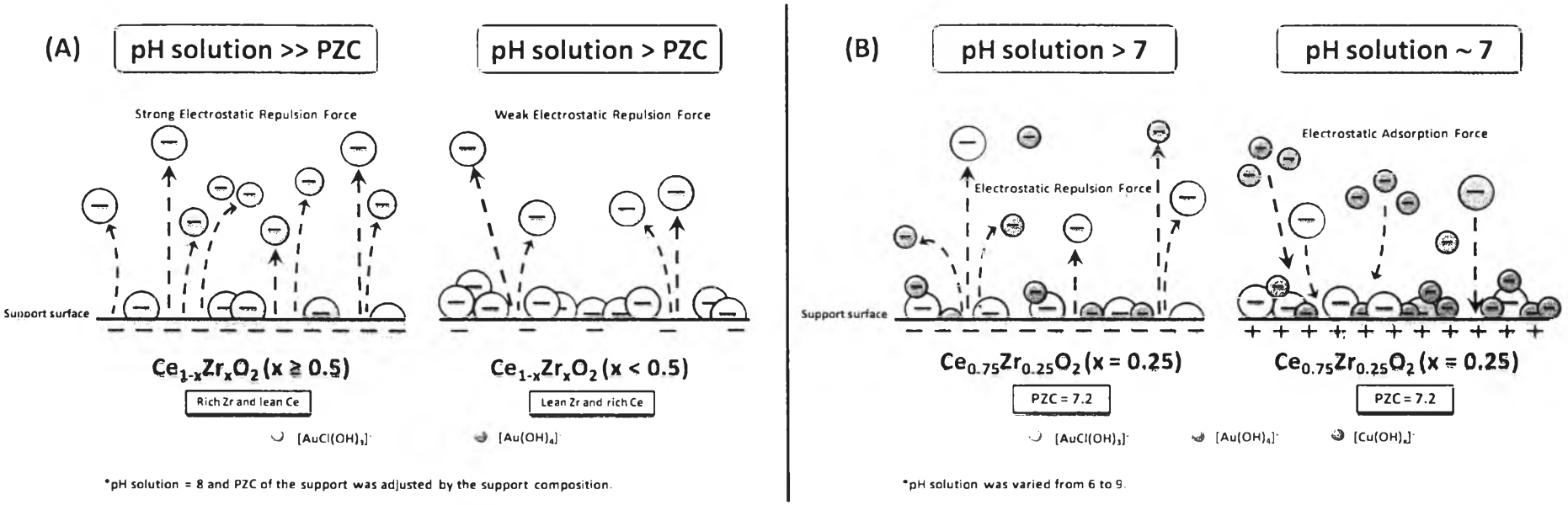

Figure 6.1 Schematic drawing of surface charge change with (A) different supports over Au/CeO_2–ZrO_2 catalysts and (B) different pH levels over Au–Cu/$Ce_{0.75}Zr_{0.25}O_2$ catalysts.

For the bimetallic catalysts (Table 6.2), the composition of Au and Cu was pH dependent. The amounts of Au and Cu increased with increasing pH from 6 to 7, and then decreased when the pH increased further. The difference in metal uptake possibly came from the retention of chloride and nitrate species of the precursors during the hydrolysis process, where the $AuCl_4^-$ species in the solution were converted to a $Au(OH)_nCl_{4-n}^-$ (n = 1–3) anion above pH 6 with n ~ 3. The extent of hydrolysis in the metal species became less pronounced at lower pH level due to decreased hydrolysis of the Au–Cl bond [31]. Similarly, this phenomenon was applicable for copper nitrate converting to copper hydroxide. As mentioned in the previous section, the PZC of $Ce_{0.75}Zr_{0.25}O_2$ (CP) was 7.20. Again, below the point of zero charge (pH < PZC) of the support, the surface charge was positive due to the protonation of the surface hydroxyls, so higher Au and Cu anion uptake was possible due to an electrostatic adsorption force [22,32]. Above the point of zero charge (pH > PZC) of the support, the surface charge was negative due to the removal of protons from the surface hydroxyls, resulting in an electrostatic repulsion force of Au and Cu anions [21,32]. Consequently, the highest gold and copper uptakes were observed at pH 7, which were in agreement with previous reports [21,33]. Moreover, the schematic drawing of the changes in the bimetallic catalysts with different pH levels is shown in Fig. 6.1B.

The lattice constant, a_0, of CeO_2–ZrO_2 was in the range of 0.532–0.542 nm, which was smaller than that of pure CeO_2 (0.544), indicating that the smaller ionic radius of Zr^{4+} (0.084 nm) had incorporated into the Ce^{4+} (0.097 nm) lattice forming $Ce_{1-x}Zr_xO_2$ solid solution [34], resulting in the shrinkage of the lattice parameter [17,35]. The lowest a_0 values were observed for $Ce_{0.5}Zr_{0.5}O_2$ (CP and SG), and the average lattice constant increased with higher ZrO_2 concentrations. This indicated the maximum Zr^{4+} incorporation was achieved at x = 0.5. For x > 0.5, segregation of Zr^{4+} from Ce^{4+} was favored giving rise to a non-uniform solid solution in the Zr-rich supports, which is in agreement with previous work [34].

Figure 6.2 shows the XRD patterns of the CeO_2–ZrO_2 catalysts with and without Au loadings. The pure CeO_2 and pure ZrO_2 were included in order to compare with CeO_2–ZrO_2 (Fig. 6.2A and B). The strongest diffraction peak of CeO_2 at $2\theta = 28.5°$ represents the fluorite cubic structure, and other weaker peaks at 33.08,

47.47, 56.33, 59.08, 69.40, 76.69, and 79.07°, respectively, correspond to (200), (220), (311), (222), (400), (331), and (420) [18]. For the CP and SG supports, only the cubic CeO_2 phase was detected without the appearance of ZrO_2 diffractions at x = 0.25. With higher Zr concentrations (x > 0.25), all CeO_2 peaks were broader with lower intensities, and they also shifted to higher theta values with the observation of ZrO_2 diffraction patterns confirming the creation of a solid solution [36]. Replacement of Ce^{4+} by the well-dispersed Zr^{4+} decreases the ceria crystallite size [36]. When adding 75% mol Zr, the crystallite size of the CeO_2 particles became larger due to the segregation of Zr^{4+} into the zirconia phase, resulting in lattice expansion of the Ce^{4+} cubic phase. Biswas et al. [36] and Masui et al. [37] also reported that the addition of 20–80% mol ZrO_2 provided high surface area CeO_2–ZrO_2, and caused structural changes in the ceria–zirconia crystallites. A similar explanation has been used with CeO_2–Fe_2O_3 catalysts [16,18]. It has also been noted that the minimum crystallite size of solid solution was not always observed at 50% mol Zr since the difference in preparation techniques could sometimes deviate or distort ceria crystal growth.

For the XRD patterns of 3 wt% Au/CeO_2–ZrO_2 catalysts (Fig. 6.2C and D), the trends of the changes in support diffractions were still the same as the pure support, suggesting that the evolution of a solid solution was independent of Au loading (or might be less pronounced). In comparison to the Au/CeO_2, the Au (111) diffraction at 38.5° became detectable at the initial Zr concentration (x = 0.25), whereas the diffractions of Au (200) at 44.4° and Au (220) at 64.6° [5] were found at high Zr concentrations (x > 0.25) for both CP and SG samples probably due to the drastic change in gold dispersion and particle size with Zr concentration. Indeed, the small Au nanoparticles (< 5 nm) might be well-dispersed in the pure CeO_2 support, so the Au crystallite size might be less than the minimum resolution of the XRD machine [5]. Au crystallite sizes were calculated from Scherrer's equation for all detectable Au diffraction planes (Table 1). The CP and SG catalysts gave similar results in that the Au crystallite sizes were enlarged with increasing amounts of Zr. The relationship between the support composition with the Au crystallite and/or particle size has been clarified in Au/CeO_2–Fe_2O_3 catalysts, where the excess Fe

increases the Au crystallite size significantly by strengthening the Au–Fe intermetallic bond to form an Au cluster (Au_n, $1 < n < 10$) which, in turn, enhances Au crystallinity [18,38]. Thus, we speculated that Zr could act the same as Fe, forming Au clusters by Au–Zr intermetallic bonding in the Zr-rich catalysts. Hence, it was reasonable to identify Au sintering in the presence of high Zr concentrations. (In terms of Au dispersion, the width of the Au diffraction could be briefly approximated as well as Ni dispersion [36].) The Au peaks had higher intensities in the 50–75% mol Zr, indicating that the Au particles were not well-dispersed on the support. At low Zr content ($x \leq 0.25$), all Au peak intensities were lower and broader, indicating good dispersion of Au crystallites on the supports. In conclusion, the Au dispersion on both CP and SG supports were ordered as following: $Au/Ce_{0.75}Zr_{0.25}O_2$ > $Au/Ce_{0.5}Zr_{0.5}O_2$ > $Au/Ce_{0.25}Zr_{0.75}O_2$, and the Au particle sizes displayed the opposite trends. Even though Au/CeO_2 has the best Au dispersion, and Au/ZrO_2 also has an intermediate Au crystallite size, we suggest that the influences of the $Ce_{1-x}Zr_xO_2$ solid solution and the Au optimum size of the catalyst had a more dominated effect. When comparing the preparation techniques, the CP technique provided better catalytic properties than the SG technique, even in the presence of Au deposition, such as uniform $Ce_{1-x}Zr_xO_2$ solid solution, smaller CeO_2 crystallite size, suitable Au crystallite and particle size, and better Au dispersion.

The XRD patterns of the 1.5 wt% Au–1.5 wt% Cu and 3 wt% Cu over CeO_2–ZrO_2 catalysts show that no peaks of any copper species, including metallic Cu, were observed (Fig. 6.3). This is only possible if the copper is highly dispersed or forming an alloy with gold [39]. Moreover, the Au (111) diffraction peaks shifted towards higher angles (38.5° to 39.78°) for all samples, indicating the formation of an Au–Cu alloy [39]. The lattice constants calculated from the alloy diffraction were between the pure gold (0.4079 nm) and pure copper (0.3615 nm), indicating that Au_xCu_{1-x} intermetallic alloys were formed [40]. The CeO_2 and Au crystallite sizes were found to be in the range of 7–9 nm and 13–15 nm, respectively. Interestingly, the bimetallic catalysts have larger crystallite sizes than those of Au catalysts, implying that the presence of Cu might inherently improve the Au crystal growth during the alloy formation.

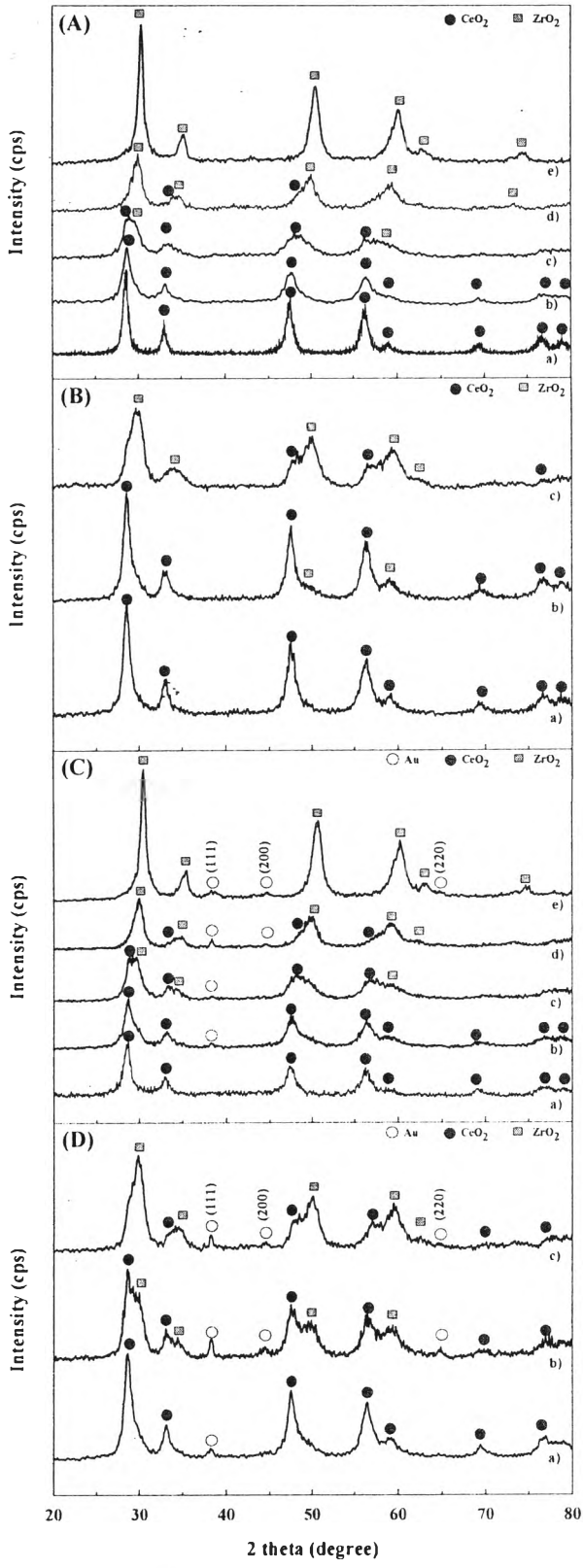
(A)
CeO2
ZrO2
e)
d)
c)
b)
a)
Intensity (cps)
(B)
CeO2
ZrO2
c)
b)
a)
Intensity (cps)
(C)
Au
CeO2
ZrO2
(111)
(200)
(220)
e)
d)
c)
b)
a)
Intensity (cps)
(D)
Au
CeO2
ZrO2
(111)
(200)
(220)
c)
b)
a)
Intensity (cps)
20
30
40
50
60
70
80
2 theta (degree)

Figure 6.2 XRD patterns of the CeO_2–ZrO_2 and Au/CeO_2–ZrO_2 catalysts calcined at 400 °C with various support compositions: (A) CP supports; (a) CeO_2, (b) $Ce_{0.75}Zr_{0.25}O_2$, (c) $Ce_{0.5}Zr_{0.5}O_2$, (d) $Ce_{0.25}Zr_{0.75}O_2$, and (e) ZrO_2; (B) SG supports; (a) $Ce_{0.75}Zr_{0.25}O_2$, (b) $Ce_{0.5}Zr_{0.5}O_2$, and (c) $Ce_{0.25}Zr_{0.75}O_2$; (C) 3 wt% Au/CP; (a) Au/CeO_2, (b) Au/$Ce_{0.75}Zr_{0.25}O_2$, (c) Au/$Ce_{0.5}Zr_{0.5}O_2$, (d) Au/$Ce_{0.25}Zr_{0.75}O_2$, and (e) Au/ZrO_2; and (D) 3 wt% Au/SG; (a) Au/$Ce_{0.75}Zr_{0.25}O_2$, (b) Au/$Ce_{0.5}Zr_{0.5}O_2$, and (c) Au/$Ce_{0.25}Zr_{0.75}O_2$.

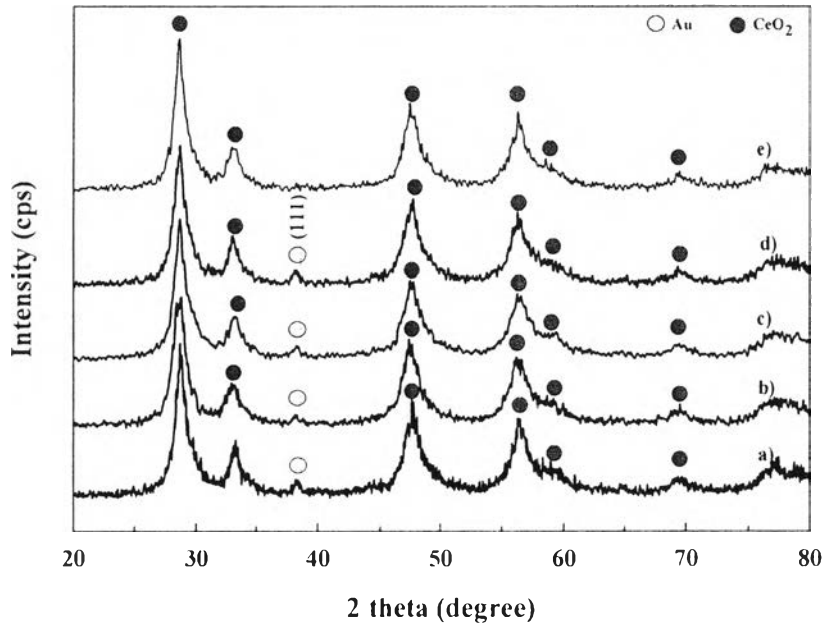

Figure 6.3 XRD patterns of Au–Cu/$Ce_{0.75}Zr_{0.25}O_2$ (CP) (1.5 wt% Au–1.5 wt% Cu) calcined at 400 °C at various pH levels: (a) pH 6; (b) pH 7; (c) pH 8; (d) pH 9; and (e) 3 wt% Cu/$Ce_{0.75}Zr_{0.25}O_2$.

UV–vis spectra measurements were used to identify the oxidation state of the Au species and the change of the support surface (Fig. 6.4). Indeed, the authors would like to apply this technique to check whether the results followed the trends of the XRD or not, after preparing the mixed oxide supports with and without Au deposition. The results show that the pure CeO_2 and ZrO_2 (not shown) have strong absorption bands at 343–345 nm and 208–210 nm, respectively [41]. For the CeO_2–ZrO_2 supports (Fig. 6.4A), neither the ZrO_2 nor the CeO_2 adsorption is observed in the range of 260–290 nm, attributing to the full connectivity of Ce–Zr–O

linkages via the incorporation of Zr into the Ce framework [42]. This implies that there was an interaction between Ce and Zr in the mixed oxides, and the formation of $Ce_xZr_{1-x}O_2$ solid solution is possible. On the other hand, the shifting of the adsorption band is the result of either the rearrangement in the electronic adsorption site [43] or the strain development [44], with respect to those of the pure phase. Other bands in the mixed oxides are attributed to the various charge transitions. For instance, the bands at 205–208 nm and 216–228 nm could be matched with the transitions of Ce^{3+} species and/or monoclinic ZrO_2, while the bands of 308, 341–343, and 351 nm are, respectively, demonstrated as the low coordination surface of $O^{2-} \rightarrow Ce^{4+}$, the transition of CeO_2, and the low coordination surface of $O^{2-} \rightarrow Ce^{3+}$ [41]. These also reveal the nonstoichiometric fluorite structure of solid solution, where various localized O–Ce charge transfers (Ce^{3+} and Ce^{4+}) might be embedded in the zirconia matrix instead [45]. However, this paper does not discuss the complex electronic effect. When focusing on the Au absorption band, the Au clusters band become visible at 280–300 nm [46,47] at Zr/Ce > 1, and only the gold plasmon or Au metallic (Au^0) band at 500–600 nm is present in the SG samples (Fig. 6.4B and C) [5,18]. The results are in line with the sintering of the Au cluster and Au metallic particles, which were found in the Zr-rich supports, and also in the SG supports.

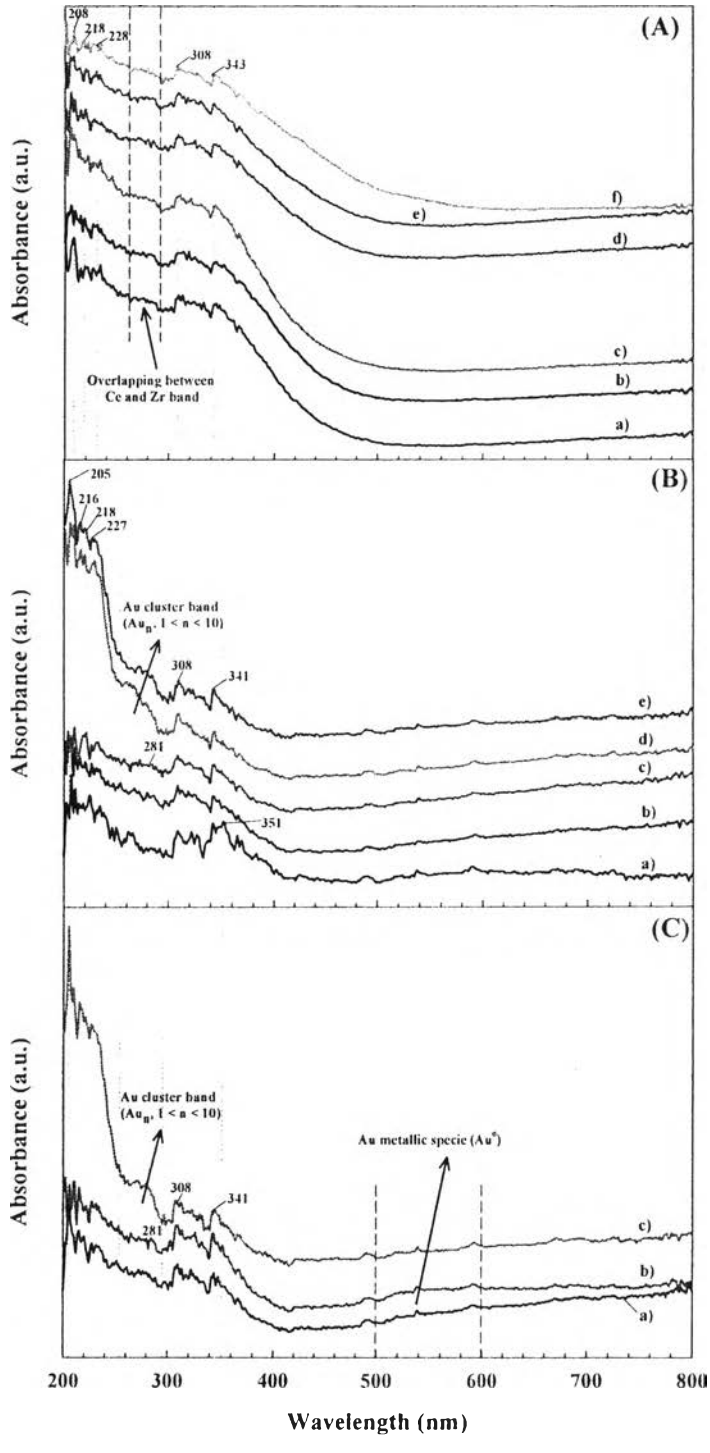

Figure 6.4 Diffuse reflectance UV–vis spectra of: (A) SG supports; (a) $Ce_{0.75}Zr_{0.25}O_2$, (c) $Ce_{0.5}Zr_{0.5}O_2$, (e) $Ce_{0.25}Zr_{0.75}O_2$; and CP supports; (b) $Ce_{0.75}Zr_{0.25}O_2$, (d) $Ce_{0.5}Zr_{0.5}O_2$, (f) $Ce_{0.25}Zr_{0.75}O_2$; (B) 3 wt% Au/CP; (a) Au/CeO_2, (b) $Au/Ce_{0.75}Zr_{0.25}O_2$, (c) $Au/Ce_{0.5}Zr_{0.5}O_2$, (d) $Au/Ce_{0.25}Zr_{0.75}O_2$, and (e) Au/ZrO_2; and

(C) 3 wt% Au/SG; (a) $Au/Ce_{0.75}Zr_{0.25}O_2$, (b) $Au/Ce_{0.5}Zr_{0.5}O_2$, and (c) $Au/Ce_{0.25}Zr_{0.75}O_2$.

Figure 6.5 shows the reduction profiles of the CeO_2–ZrO_2 and Au/CeO_2–ZrO_2 catalysts. Focusing on the support reduction (Fig. 6.5A and B), the pure CeO_2 represents a low-temperature peak at 486 °C, which is attributed to the reduction of the oxygen on the ceria surface, and a high-temperature peak at 818 °C corresponds to the bulk reduction ($CeO_2 \rightarrow Ce_3O_4$) [5,18]. No reduction peak was observed on the pure ZrO_2 support. In addition, the area under both surface and bulk reduction peaks of the $Ce_{1-x}Zr_xO_2$ (CP) samples declined progressively with increasing Zr content, representing decreasing amounts of Ce^{4+} species. Likewise, the disappearance of the bulk reduction was possible for the lowest Ce content. In the Zr-rich sample ($Ce_{0.25}Zr_{0.75}O_2$), CeO_2 was dispersed thoroughly on the surface only, which resulted in a total reduction of CeO_2 [36]. The high H_2 consumption of the $Ce_{0.75}Zr_{0.25}O_2$ (CP) could be attributed to the better reducibility, resulting in better redox properties as well as better thermal stability of the catalyst. Furthermore, the position of the surface reduction peak shifted from 486 to 565 °C, indicating that the Ce–Zr interaction was improved with increasing Zr as well. The higher the reduction temperature, the stronger the Ce–Zr interaction to form the solid solution, which followed the same trends as XRD [36]. Interestingly, the additional weak peak at 410 °C was ascribed to the reduction of adsorbed surface oxygen species on the free ceria particles [48]. However, the bulk reduction shows a slight difference of shifting behavior. We postulated that the main interaction initially occurred on the ceria surface during the incorporation of Zr^{4+} inside the Ce^{4+} lattice. There are some publications reporting the phase change of $Ce_{1-x}Zr_xO_2$ solid solution when varying the Ce/Zr ratio [36,49]. Unfortunately, our results do not allow for the determination of the variety of phases.

According to the TPR profiles in the SG supports (Fig. 6.5B), the shifting behavior of $Ce_{1-x}Zr_xO_2$ reduction peaks followed the same trends as the CP samples. Interestingly, additional shoulders occurred at lower reduction temperatures (388, 455, and 475 °C) near the surface reduction, which were defined as the

existence of Ce^{4+} located in different chemical environment, such as the subsurface region [50]. In comparison to the Zr-rich samples ($x \geq 0.5$) in CP, the bell shape of the bulk reductions (833 and 787 °C) were also detected with the narrow peaks in SG, probably due to the irregular or narrow dispersion of the bulk ceria particles as a consequence of a less uniform solid solution phase. Based on our knowledge, these abnormal reduction shapes indicated the incomplete incorporation of Zr, resulting in a non-uniform solid solution phase and a change in Ce–Zr bonding. This was why more free ZrO_2 particles remained on the surface, causing higher crystallite size without shrinking the lattice, as confirmed by XRD. In conclusion, the CP technique was more useful than SG for providing better properties for the support in cases of uniform $Ce_{1-x}Zr_xO_2$ phase, Ce–Zr interaction, reducibility, and dispersion.

In Fig. 6.5C and D, the Au/CeO_2–ZrO_2 catalysts show the reductions of the surface and the bulk also appeared at 512–570 °C and 765–825 °C, respectively, while the lowest reduction temperature range of 100–150 °C corresponded to the reduction behavior of the Au_xO_y or $Au^{\delta+}$ to Au metallic specie (Au^0) [50]. Two reduction peaks were found in $Au/Ce_{0.75}Zr_{0.25}O_2$ (CP), attributing to the reduction of two classified Au cationic species: (i) $Au^{3+} \rightarrow Au^0$ at 122 °C and (ii) $Au^+ \rightarrow Au^0$ at 149 °C [51,52]. In fact, the area under the Au reduction peak briefly approximated the amount of $Au^{\delta+}$ species, where the large amounts of less reductive Au species (Au^0 or Au_n) could suppress the area and promote Au sintering [18]. This coincided with Au sintering at high Zr concentrations, while the rich Ce samples contained more $Au^{\delta+}$. When focusing on the interaction site, the Au peaks shifted toward higher temperatures with the addition of more Zr, indicating that the Au–support interaction was improved. For the Zr rich catalysts, the Au peaks conversely shifted to lower temperatures, probably due to Au sintering which favored the Au–Au interaction to form larger particles instead. It can be suggested that the activity of the catalysts strongly depended on the $Au^{\delta+}$ present on the surface, the Au sintering, and the strength of the Au interaction. However, the active Au species for the SRM has not been clarified [12].

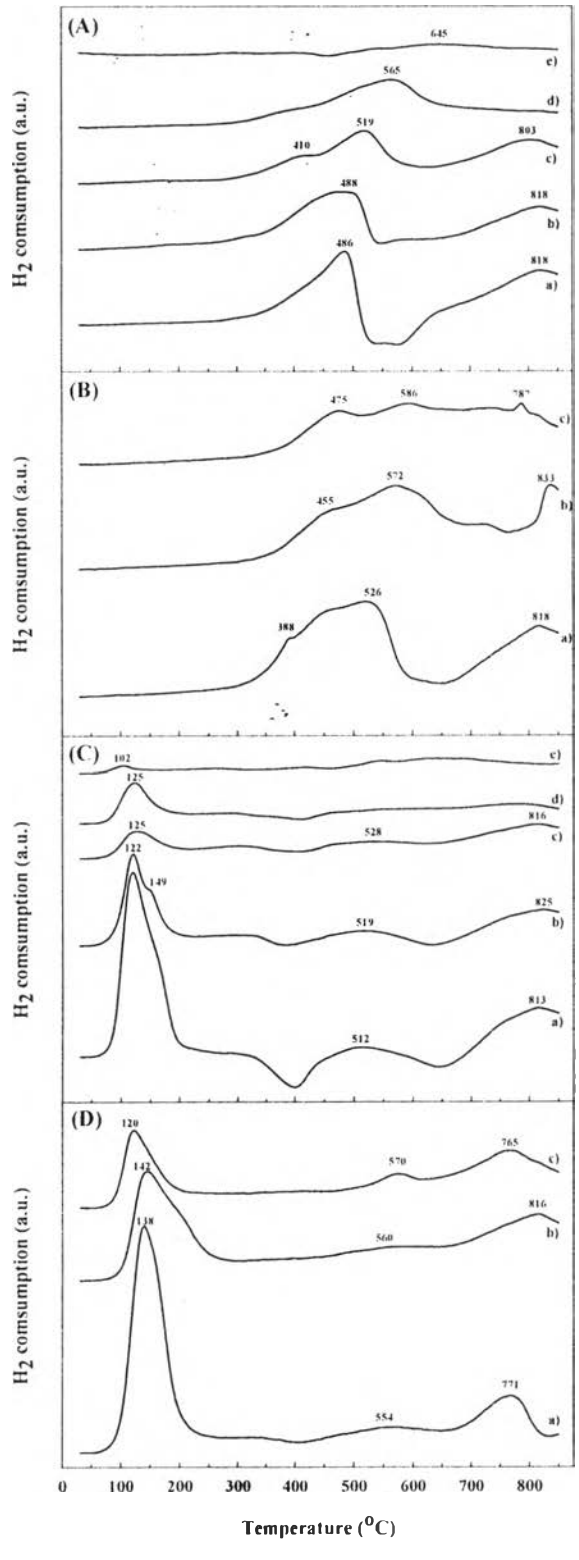

Figure 6.5 TPR profiles of: (A) CP supports; (a) CeO_2, (b) $Ce_{0.75}Zr_{0.25}O_2$, (c) $Ce_{0.5}Zr_{0.5}O_2$, (d) $Ce_{0.25}Zr_{0.75}O_2$, and (e) ZrO_2; (B) SG supports; (a) $Ce_{0.75}Zr_{0.25}O_2$, (b) $Ce_{0.5}Zr_{0.5}O_2$, and (c) $Ce_{0.25}Zr_{0.75}O_2$; (C) 3 wt% Au/CP; (a) Au/CeO_2, (b)

$Au/Ce_{0.75}Zr_{0.25}O_2$, (c) $Au/Ce_{0.5}Zr_{0.5}O_2$, (d) $Au/Ce_{0.25}Zr_{0.75}O_2$, and (e) Au/ZrO_2; and (D). 3 wt% Au/SG; (a) $Au/Ce_{0.75}Zr_{0.25}O_2$, (b) $Au/Ce_{0.5}Zr_{0.5}O_2$, and (c) $Au/Ce_{0.25}Zr_{0.75}O_2$.

According to the TPR profiles of the 1.5 wt% Au–1.5 wt% Cu over CeO_2–ZrO_2 and Cu/CeO_2–ZrO_2 catalysts (Fig. 6.6), the Cu/CeO_2–ZrO_2 showed the low temperature peak of 155 °C corresponding to the reduction of highly dispersed or small CuO particles strongly interacting with the support, while the peak at 183 °C represents the reduction of the bulk or larger CuO particles which had a weaker support interaction [53]. The significant increase in intensities of the bimetallic catalysts at T_{max} < 200 °C with simultaneously decreasing intensity of the support reduction (not shown here) was attributed to either the excess H_2 spilling over the reactive sites prompted by CuO_x species [21], or the existence of Cu–Ce–O solid solution [54]. Furthermore, the presence of Cu led to a shift of the Au reduction towards higher temperatures (159–168 °C), corresponding to the strong interaction between Au_xO_y and highly dispersed CuO_x to form alloy particles [22]. The appearance of a symmetric reduction peak indicated a homogeneous $AuCu_x$ alloy, which was similar to that of Pd–Cu alloy catalyst [55]. However, at pH 8 a non-uniform alloy phase was due to the presence of two visible reduction peaks, which was matched with the alloy reduction and the isolated bulk CuO remaining on the surface of the catalyst. The shifting behavior of the bimetallic reduction can also be assigned to the change in alloy size [56]. The small particles could be reduced easier than the larger ones. Consequently, the pH 7 catalyst provided the smallest alloy size due to the simple reduction. Nonetheless, the fluctuation of the alloy size was observed with varying pH values, so TEM was then used to detect the true size. In conclusion, the smallest uniform alloy in the bimetallic catalyst at pH 7 might be active for the SRM activity.

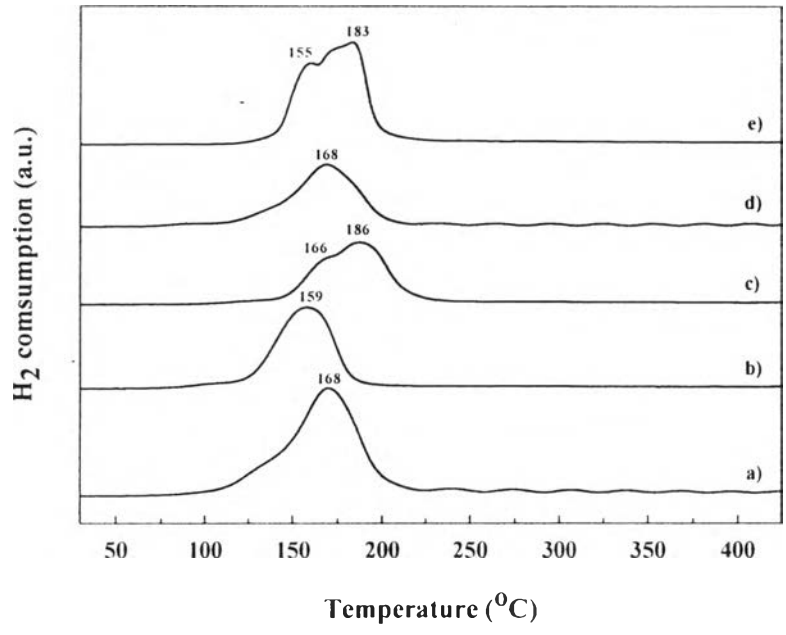

Figure 6.6 TPR profiles of Au–Cu/$Ce_{0.75}Zr_{0.25}O_2$ (CP) (1.5 wt% Au–1.5 wt% Cu) at various pH levels: (a) pH 6; (b) pH 7; (c) pH 8; (d) pH 9; and (e) 3 wt% Cu/$Ce_{0.75}Zr_{0.25}O_2$.

TEM images were also used to evaluate the Au particle sizes—the dark spots on the supports—and their distribution, as imaged in Fig. 6.7. The mean Au particle sizes of the Au/CeO_2 and the Au/ZrO_2 were 4.86 and 35.64 nm, respectively. For the Au/CeO_2–ZrO_2 (CP) catalysts, large differences in particle sizes were observed as following: Au/$Ce_{0.75}Zr_{0.25}O_2$ (30.16 nm) < Au/$Ce_{0.5}Zr_{0.5}O_2$ (57.72 nm) < Au/$Ce_{0.25}Zr_{0.75}O_2$ (61.02 nm). The SG catalysts also had similar trends (not shown here), where Au/$Ce_{0.75}Zr_{0.25}O_2$, Au/$Ce_{0.5}Zr_{0.5}O_2$, and Au/$Ce_{0.25}Zr_{0.75}O_2$ were 51.49, 71.82, and 74.56 nm, respectively, but the Au particle sizes were much larger in the same Ce/Zr ratio, representing the complete agglomeration of Au nanoparticles. The results were in accordance with many previous characterizations, where Au sintering was strongly affected by high Zr concentrations for all samples. Besides, this observation implied that the better dispersion of Au particles belonged to the Au/$Ce_{0.75}Zr_{0.25}O_2$ (CP) due to its narrow distribution of small Au particles. In contrast, lower Au dispersion with higher Zr concentrations was the consequence of Au sintering. We postulated the suitable Au particle size at 30.16 nm—obtained by

the CP technique—was the most suitable for the SRM reaction. In order to better understand the growth of Au particle size with increasing Zr concentrations, the strong interaction between the $[Au(OH)_4]^-$ and the hydrogen-bonded hydroxyl on ZrO_2 have dominated to form Au clusters that nucleated and grew to large Au particles in the catalyst. This phenomenon appeared with increasing Zr. The same mechanism of metal growth has already been reported by Qian et al. [25], who found the aggregation of Au nanoparticles formed larger particles after increasing the CoO concentration in the $Au/CoO/SiO_2$ catalyst. The gold precursor favorably deposited with the hydrogen-bonded hydroxyls in $Co(OH)_2$ on SiO_2 to form large Au cluster species. In this experiment, the nucleation of the Au particle size in the Au/CeO_2–ZrO_2 (CP and SG) catalysts could behave similarly in the presence of high Zr concentrations, even in the presence of low Au loading. The influence of surface hydroxyls on the oxides was an important factor for the Au particle size, while the distribution of surface hydroxyls on the oxides was not discussed in this paper.

The Au–Cu particles were formed homogeneously and difficult to identify (Fig. 6.8), and were measured altogether to get the mean average. The average Au–Cu particle size was, respectively, approximated at 68.13 (pH 6), 31.48 (pH 7), 36.16 (pH 8), and 42.54 (pH 9) nm (Fig. 6.8a–d). It seems that the combination of copper and gold helped enlarge the alloy particle sizes. The largest alloy particle size was found in the lowest pH of 6; the increase of pH (7–9) caused smaller alloy particle sizes. This observation suggests that the size of the Au–Cu alloy, while with pH dependent, could be related with the agglomeration of alloy particles and/or Au agglomeration into larger sizes, which was the main factor why the alloy particles exhibit different catalytic activity. The larger the alloy particle size, the more the sintering. This size effect was in agreement with the TPR and XRD results. Therefore, the pH condition of 7 was the suitable condition for preventing alloy sintering during the preparation step due to its lowest particle size, which was close to the size of $Au/Ce_{0.75}Zr_{0.25}O_2$ (CP). The impact of the size was less and revealed the advantage of Cu addition in terms of preventing Au agglomeration (Fig. 6.8b). Liu et al. have proposed a core-shell model in both Au–Ag [57] and Au–Cu [39] bimetallic catalysts where the CuO or AgO formed a shell on the gold particles, so they could inhibit the aggregation of Au particles during the calcination

step. Likewise, the Au–Cu/CeO_2–ZrO_2 catalysts could be the same model as this synergistic effect, where some part of CuO preserved the Au particles by forming a shell, and some formed alloys with the Au particles.

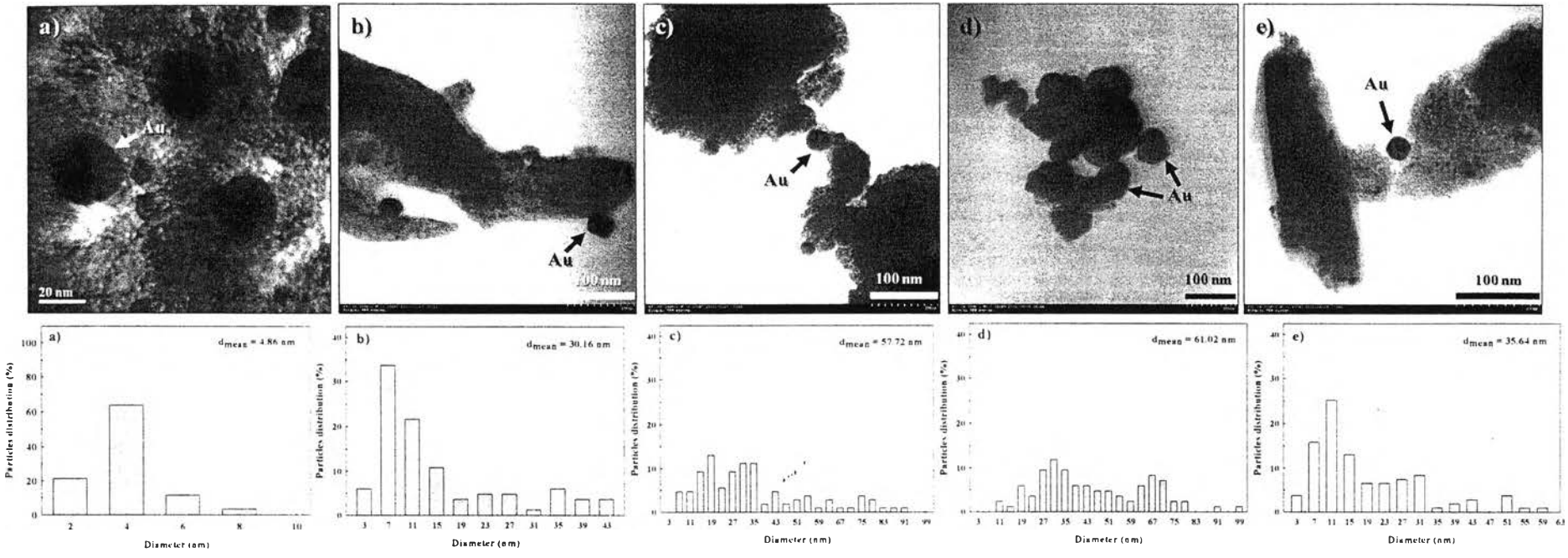

Figure 6.7 TEM images and Au particle size distributions of $Au/CeO_2–ZrO_2$ catalysts: (a) Au/CeO_2; (b) $Au/Ce_{0.75}Zr_{0.25}O_2$ (CP); (c) $Au/Ce_{0.5}Zr_{0.5}O_2$ (CP): (d) $Au/Ce_{0.25}Zr_{0.75}O_2$ (CP); and (e) Au/ZrO_2.

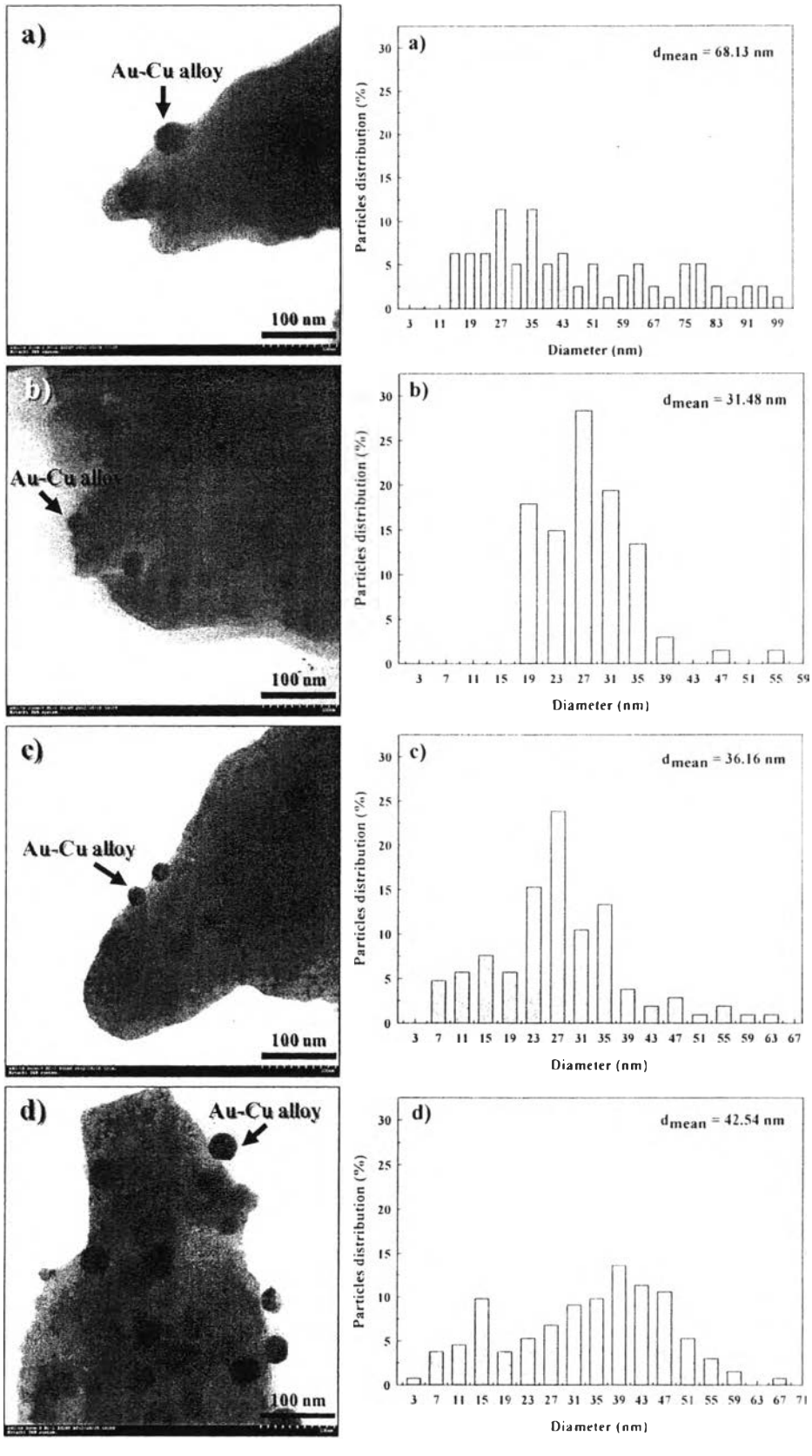

Figure 6.8 TEM images and Au particle size distributions of Au–Cu/CeO_2–ZrO_2 catalysts: (a) pH 6; (b) pH7; (c) pH 8; and (d) pH 9.

6.4.2 Catalytic activity

6.4.2.1 Effect of catalyst preparation and support composition

Figure 6.9 presents the catalytic activities of the supports and supported Au catalysts. An increase of methanol conversion with a reaction temperature increase was observed in all samples, according to the endothermic reaction which was more favorable at high temperatures. The pure CeO_2 support exhibited higher catalytic activity than the pure ZrO_2 support, while the mixed oxide supports in $Ce_{0.75}Zr_{0.25}O_2$ (CP) gave the highest methanol conversion (Fig. 6.9A) and product gas concentrations (Fig. 6.9B). The CO concentration was 0–5 % for temperatures below 350 °C, and increased to 18% at the highest temperature (500 °C), indicating that methanol decomposition was pronounced [18]. The highest H_2 concentration occurred on the $Ce_{0.75}Zr_{0.25}O_2$ (CP) support, where it exceeded 60 % at the highest temperature. When comparing the gas selectivity of the $Ce_{0.75}Zr_{0.25}O_2$ (CP) support with and without Au loading (Fig. 6.9C and D), it can be seen that the presence of Au decreases CO selectivity and increases H_2 selectivity particularly at low temperatures. In terms of CO_2 selectivity, the $Ce_{0.75}Zr_{0.25}O_2$ support was found in the range of 12–20 %, while the presence of Au gave much higher selectivity (15–68 %) in the whole range of reaction temperature. It was noted that the CO_2 selectivity decreased with increasing CO selectivity after increasing the reaction temperature, indicating that more CO was also formed by the methanol decomposition, which was favorable at high temperatures.

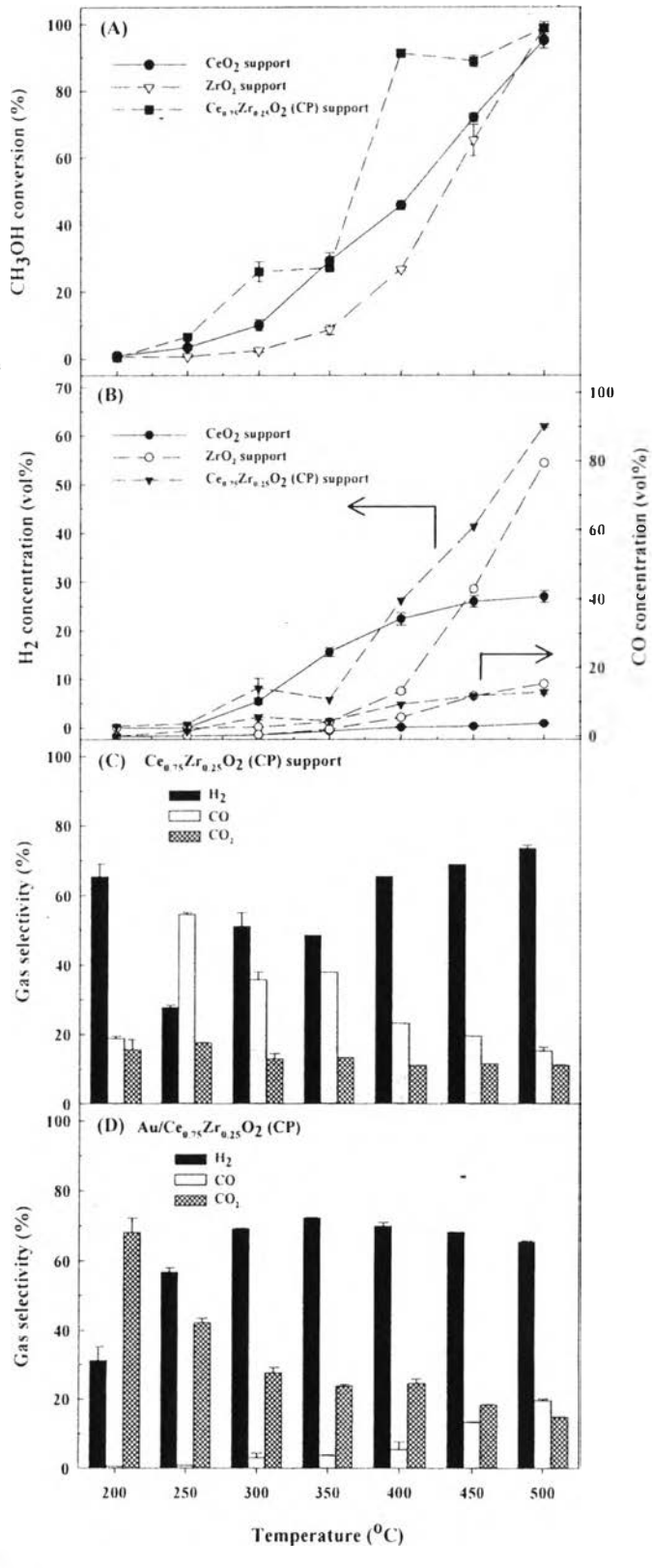

Figure 6.9 Effect of support composition without Au deposition on (A) methanol conversion and (B) product composition. Gas selectivity: (C) without Au deposition;

and (D) with Au deposition. (Reaction conditions: H_2O/CH_3OH, 2/1; calcination temperature, 400 °C.)

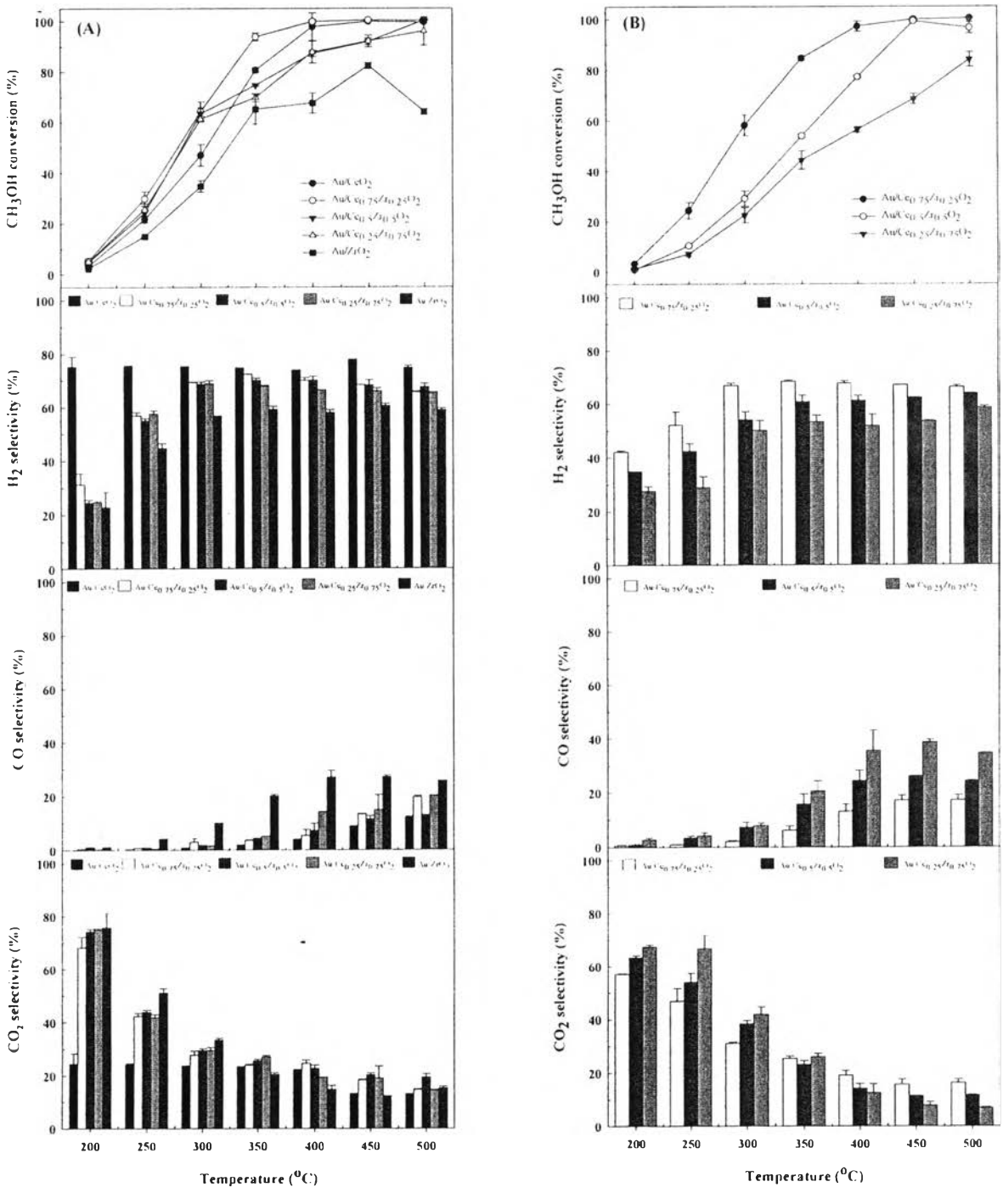

Figure 6.10 Catalytic activities of (A) 3 wt% Au/CP and (B) 3 wt% Au/SG catalysts. (Reaction conditions: H_2O/CH_3OH, 2/1; calcination temperature, 400 °C.)

When comparing the catalytic activities of 3 wt% $Au/Ce_{1-x}Zr_xO_2$ catalysts, as shown in Fig. 6.10, the Au catalysts exhibited much better catalytic performance than those of the supports, which indicates that the addition of the active Au metal was important for efficiently promoting SRM activity. The SRM activity was strongly enhanced by the Zr addition as ordered: $Au/Ce_{0.75}Zr_{0.25}O_2$ > $Au/Ce_{0.5}Zr_{0.5}O_2$ > $Au/Ce_{0.25}Zr_{0.75}O_2$. Both CP and SG samples obtained the highest catalytic activities with the lowest Zr content, whilst the Zr-rich support suppressed the SRM activity. In addition, the H_2 yield showed the same trend as the methanol conversion. When interpreting all characterization results, the CP samples gave much higher activity because of the uniform solid solution phase and reduced Au sintering.

6.4.2.2 Effect of bimetallic catalyst

The catalytic activity of all samples after loading Cu, are illustrated in Fig. 6.11. The SRM activity increased substantially with the initial increase of pH from 6 to 7, and its activity dropped with further increasing pH > 7. Full methanol conversion at pH 7 was found at 350 °C, and close to the pure $Cu/Ce_{0.75}Zr_{0.25}O_2$ (CP) catalyst. The CO_2 selectivity of all samples was in the range of 10–65 %. Hydrogen selectivity was enhanced to 75–80 %, and very low CO selectivity at 200–300 °C was observed, indicating that the Au–Cu catalyst facilitated SRM and CO reduction. The difference in activity mainly came from the different alloy properties in terms of homogeneity and size. The suitable properties for the bimetallic catalysts in SRM were the strong (but not the strongest) interaction of Au and the highly dispersed CuO to form homogeneous $AuCu_x$ alloy with small particle size. Some research mentions that the Cu^{2+} or Cu^{+} plays an inactive site for the reaction, while Cu^0 was active [53]; however, the electronic states of the Cu species were not identified in this experiment.

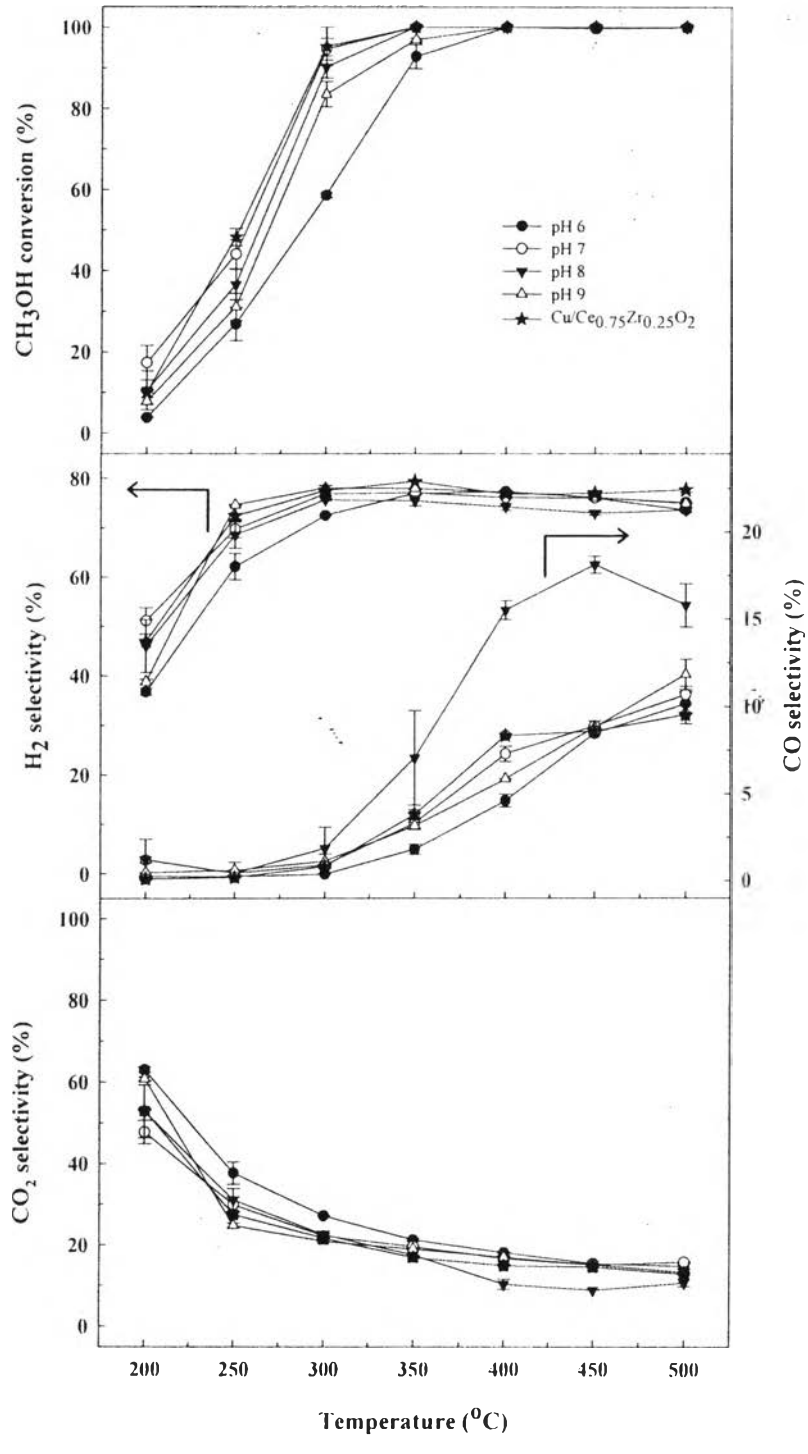

Figure 6.11 Effect of pH levels on methanol conversion and product composition over Au–Cu/$Ce_{0.75}Zr_{0.25}O_2$ (CP) catalysts. (Reaction conditions: H_2O/CH_3OH, 2/1; calcination temperature, 400 °C.)

6.5 Conclusions

The Au–Cu/CeO_2–ZrO_2 catalysts were developed with different support preparation routes for SRM. High SRM activity was initially obtained in both CP and SG supports with the optimum Zr amount at 25 %mol due to the incorporation of Zr^{4+} into the Ce^{4+} lattice to form the uniform $Ce_{0.75}Zr_{0.25}O_2$ solid solution phase. The increase in Zr concentrations negatively caused (i) large Au particle sizes, which came from the interaction of the Au precursor and the hydrogen-bonded hydroxyl on the ZrO_2 surface to form Au clusters, and (ii) non-uniform $Ce_{1-x}Zr_xO_2$ phase, which suppressed catalytic performance. The CP technique provided better solid solution and Au particle size for SRM. The role of Cu in the bimetallic catalyst (1.5 wt% Au and 1.5 wt% Cu) at pH 7 was to preserve the small alloy size and form a strong Au–Cu alloy interaction, significantly promoting SRM activity. It was evidenced by complete methanol conversion and high H_2 purity with a low CO concentration. However, the best activity in the pH 7 Au–Cu catalyst was still close to the individual Cu catalyst. Further research need to be conducted in the Au/Cu atomic ratio, calcination temperature, and gas pretreatment in the future work.

6.6 Acknowledgments

The authors acknowledge the contributions and financial support of the following organizations: the Thailand Research Fund through the Royal Golden Jubilee Ph.D. Program (Grant No. PHD/0282/2552); the National Center of Excellence for Petroleum, Petrochemicals, and Advanced Materials, Chulalongkorn University; and The National Research University Project of CHE and the Ratchadaphiseksomphot Endowment Fund (EN276B).

6.7 References

[1] Creutz C, Fujita E. Carbon Dioxide as a Feedstock, Carbon Management, The National Academic Press; 2001.

[2] Ocampo F, Louis B, Kiwi-Minsker L, Roger AC. Effect of Ce/Zr composition and noble metal promotion on nickel based $Ce_xZr_{1-x}O_2$ catalysts for carbon dioxide methanation. Appl Catal A 2011; 392: 36–44.

[3] Razeghi A, Khodadadi A, Ziaei-Azad H, Mortazavi Y. Activity enhancement of Cu-doped ceria by reductive regeneration of $CuO–CeO_2$ catalyst for preferential oxidation of CO in H_2-rich streams. Chem Eng J 2010; 164: 214–20.

[4] Guo Q, Chen S, Liu Y, Wang Y. Stability of Co–Ce–Mn mixed-oxide catalysts for CO preferential oxidation in H_2-rich gases. Chem Eng J 2010; 165: 846–50.

[5] Pojanavaraphan C, Luengnaruemitchai A, Gulari E. Hydrogen production by oxidative steam reforming of methanol over Au/CeO_2 catalysts. Chem Eng J 2012; 192: 105–13.

[6] Thormann J, Pfeifer P, Kunz U. Dynamic performance of hexadecane steam reforming in a microstructured reactor. Chem Eng J 2012; 191: 410–5.

[7] Thormann J, Pfeifer P, Schubert K, Kunz U. Reforming of diesel fuel in a micro reactor for APU systems. Chem Eng J 2008; 135: S74–S81.

[8] Biswas P, Kunzru D. Oxidative steam reforming of ethanol over Ni/CeO_2-ZrO_2 catalyst. Chem Eng J 2008; 136: 41–9.

[9] Huang TJ, Chen HM. Hydrogen production via steam reforming of methanol over $Cu/(Ce,Gd)O_{2-x}$ catalysts. Int J Hydrogen Energy 2010; 35: 6218–26.

[10] Huang G, Liaw BJ, Jhang CJ, Chen YZ. Steam reforming of methanol over $CuO/ZnO/CeO_2/ZrO_2/Al_2O_3$ catalysts. Appl Catal A 2009; 358: 7–12.

[11] Yi N, Si R, Saltsburg H, Stephanopoulos MF. Steam reforming of methanol over ceria and gold-ceria nanoshapes. Appl Catal B 2010; 95: 87–92.

[12] Bond GC, Louis C, Thompson DT. Catalysis by Gold, volume 6, Imperial College Press, London, 2006.

[13] Grisel R, Weststrate KJ, Gluhoi A, Nieuwenhuys BE. Catalysis by gold nanoparticles. Gold Bull 2002; 35: 39–45.

[14] Lenite BA, Galletti C, Specchia S. Studies on Au catalysts for water gas shift reaction. Int J Hydrogen Energy 2011; 36: 7750–8.

[15] Srinivas D, Satyanarayana CVV, Potdar HS, Ratnasamy P. Structural studies on NiO-CeO_2-ZrO_2 catalysts for steam reforming of ethanol. Appl Catal A 2003; 246: 323.

[16] Tabakova T, Avgouropoulos G, Papavasiliou J, Manzoli M, Boccuzzi F, Tenchev K, Vindigni F, Ioannides T. CO-free hydrogen production over Au/CeO_2–Fe_2O_3 catalysts: Part 1. Impact of the support composition on the performance for the preferential CO oxidation reaction. Appl Catal B 2011; 101: 256–65.

[17] Reddy BM, Khan A. Nanosized CeO_2–SiO_2, CeO_2–TiO_2, and CeO_2–ZrO_2 mixed oxides: Influence of supporting oxide on thermal stability and oxygen storage properties of ceria. Catal Surv from Asia 2005; 9: 155–71.

[18] Pojanavaraphan C, Luengnaruemitchai A, Gulari E. Effect of support composition and metal loading on Au catalyst activity in steam reforming of methanol. Int J Hydrogen Energy 2012; 37: 14072–84.

[19] Martinez-Arias A, Fernandez-Garcia M, Belver C, Conesa JC, Soria J. EPR study on oxygen handling properties of ceria, zirconia and Zr–Ce (1 : 1) mixed oxide samples. Catal Lett 2000; 65: 197–203.

[20] Mamontov E, Egami T, Brezny R, Koranne M, Tyagi S. Lattice defects and oxygen storage capacity of nanocrystalline ceria and ceria-zirconia. J Phys Chem B 2000; 104: 11110–6.

[21] Ou TC, Chang FW, Selva Roselin L. Production of hydrogen via partial oxidation of methanol over bimetallic Au–Cu/TiO_2 catalysts. J Mol Catal A: Chem. 2008; 293: 8–16.

[22] Chang FW, Ou TC, Selva Roselin L, Chen WS, Lai SC, Wu HM. Production of hydrogen by partial oxidation of methanol over bimetallic Au–Cu/TiO_2–Fe_2O_3 catalysts. J Mol Catal A: Chem. 2009; 313: 55–64.

[23] Pongstabodee S, Monyanon S, Luengnaruemitchai A. Hydrogen production via methanol steam reforming over Au/CuO, Au/CeO_2, and Au/CuO–CeO_2 catalysts prepared by deposition–precipitation. Ind Eng Chem Res 2012; 18: 1272–9.

[24] Thammachart M, Meeyoo V, Risksomboon T, Osuwan S. Catalytic activity of CeO_2–ZrO_2 mixed oxide catalysts prepared via sol–gel technique: CO oxidation. Catal Today 2001; 68: 53–61.

[25] Qian K, Fang J, Huang W, He B, Jiang Z, Ma Y, Wei S. Understanding the deposition–precipitation process for the preparation of supported Au catalysts. J Mol Catal A: Chem 2010; 320: 97–105.

[26] Zanella R, Delannoy L, Louis C. Mechanism of deposition of gold precursors onto TiO_2 during the preparation by cation adsorption and deposition–precipitation with NaOH and urea. Appl Catal A 2005; 291: 62–72.

[27] Casaletto MP, Longo A, Venezia AM, Martorana A, Prestianni A. Metal-support and preparation influence on the structural and electronic properties of gold catalysts. Appl Catal A 2006; 302: 309–16.

[28] Lee SJ, Gavriilidis A. Supported Au catalysts for low-temperature CO oxidation prepared by impregnation. J Catal 2002; 206: 305–13.

[29] Siddiquey IA, Furusawa T, Hoshi YI, Ukaji E, Kurayama F, Sato M, Suzuki N. Silica coating of CeO_2 nanoparticles by a fast microwave irradiation method. Appl Surf Sci 2008; 255: 2419–24.

[30] Tseng TY, Huang JM, Lin JG, Lin YL. Rheological properties of the aqueous zirconia/colloidal zirconia binder sol system. J Mater Sci 1989; 24: 2735–8.

[31] Haruta M. Size- and support-dependency in the catalysis of gold. Catal Today 1997; 36: 153–66.

[32] Ivanova S, Pitchon V, Petit C. Application of the direct exchange method in the preparation of gold catalysts supported on different oxide materials. J Mol Catal A: Chem 2006; 256: 278–83.

[33] Moreau F, Bond GC. Preparation and reactivation of Au/TiO_2 catalysts. Catal Today 2007; 122: 260–5.

[34] Zhang F, Chen CH. Phases in Ceria–Zirconia Binary Oxide $(1-x)CeO_2$–$xZrO_2$ Nanoparticles: The Effect of Particle Size. J Am Ceram Soc 2006; 89: 1028–36.

[35] Yashima M, Arashi H, Kakihana M, Yoshimura M. Application of an ion-packing model based on defect clusters to zirconia solid solutions: I, Modeling and Local Structure of Solid Solutions. J Am Ceram Soc 1992; 75: 1541–9.

[36] Biswas P, Kunzru D. Steam reforming of ethanol for production of hydrogen over Ni/CeO_2–ZrO_2 catalyst: Effect of support and metal loading. Int J Hydrogen Energy 2007; 32: 969–80.

[37] Masui T, Fujiwara K, Peng Y, Sakata T, Machida K, Mori H, Adachi G. Characterization and catalytic properties of CeO_2–ZrO_2 ultrafine particles prepared by the microemulsion method. J Alloys Compd 1998; 269: 116–22.

[38] Andreeva D, Tabakova T, Idakiev V, Christov P, Giovanoli R. Au/α–Fe_2O_3 catalyst for water–gas shift reaction prepared by deposition–precipitation. Appl Catal A 1998; 169: 9–14.

[39] Liu X, Wang A, Zhang T, Su DS, Mou CY. Au–Cu alloy nanoparticles supported on silica gel as catalyst for CO oxidation: Effects of Au/Cu ratios. Catal Today 2011; 160: 103–8.

[40] Chimentão RJ, Medina F, Fierro JLG, Llorca J, Sueiras JE, Cesteros Y, Salagre P. Propene epoxidation by nitrous oxide over Au–Cu/TiO_2 alloy catalysts. J Mol Catal A: Chem 2007; 274: 159–68.

[41] Ranga Rao G, Ranjan Sahu H. XRD and UV-Vis diffuse reflectance analysis of CeO_2-ZrO_2 solid solutions synthesized by combustion method. J Chem Sci 2001; 113: 651–8.

[42] Chen HR, Shi JL, Chen TD, Yan JN, Yan DS. Preparation and characteristics of the ordered porous zirconia containing cerium. Mater Lett 2002; 54: 200–4.

[43] Coronado JM, Maira AJ, Arias AM, Conesa JC, Soria J. EPR study of the radicals formed upon UV irradiation of ceria-based photocatalysts. J Photochem Photobiol A 2002; 150: 213–21.

[44] Escribano VS, Lopez EF, Panizza M, Resini C, Amores JMG, Busca G. Characterization of cubic ceria–zirconia powders by X-ray diffraction and vibrational and electronic spectroscopy. Solid State Sci 2003; 5: 1369–76.

[45] Bensalem A, Bozon-Verduraz F, Delamar M, Bugli G. Preparation and characterization of highly dispersed silica-supported ceria. Appl Catal A 1995; 121: 81–93.

[46] Park S, Yoo K, Park HJ, Lee JC, Lee JH. Rapid gold ion recovery from wastewater by photocatalytic ZnO nanopowders. J Electroceram 2006; 17: 831–34.

[47] Souza KR, Lima AFF, Sousa FF, Appel LG. Preparing Au/ZnO by precipitation–deposition technique. Appl Catal A 2008; 340: 133–139.

[48] Liu N, Yuan Z, Wang S, Zhang C, Wang S, Li D. Characterization and performance of a ZnO–$ZnCr_2O_4$/CeO_2–ZrO_2 monolithic catalyst for methanol auto-thermal reforming process. Int J Hydrogen Energy 2008; 33: 1643–51.

[49] Pengpanich S, Meeyoo V, Rirksomboon T, Bunyakiat K. Catalytic oxidation of methane over CeO_2-ZrO_2 mixed oxide solid solution catalysts prepared via urea hydrolysis. Appl Catal A 234 (2002) 221–33.

[50] Dobrosz-Gómez I, Gómez-García MÁ, Rynkowski JM. CO oxidation over Au/CeO_2–ZrO_2 catalysts: The effect of the support composition of the Au–support interaction. Kinet Catal 2010; 51: 823–7.

[51] Chang FW, Roselin LS, Ou TC. Hydrogen production by partial oxidation of methanol over bimetallic Au–Ru/Fe_2O_3 catalysts. Appl Catal A 2008; 334: 147–55.

[52] Gluhoi AC, Tang X, Marginean P, Nieuwenhuys BE. Characterization and catalytic activity of unpromoted and alkali (earth)-promoted Au/Al_2O_3 catalysts for low-temperature CO oxidation. Top Catal 2006; 39: 101–10.

[53] Pérez-Hernández R, Gutiérrez-Martínez A, Gutiérrez-Wing CE. Effect of Cu loading on CeO_2 for hydrogen production by oxidative steam reforming of methanol. Int J Hydrogen Energy 2007; 32: 2888–94.

[54] Yaseneva P, Pavlova S, Sadykov V, Moroz E, Burgina E, Dovlitova L, Rogov V, Badmaev S, Belochapkin S, Ross J. Hydrogen production by steam reforming of methanol over Cu–$CeZrYO_x$-based catalysts. Catal Today 2008; 138: 175–82.

[55] Kugai J, Miller JT, Guo N, Song C. Role of metal components in Pd–Cu bimetallic catalysts supported on CeO_2 for the oxygen-enhanced water gas shift. Appl Catal B 2011; 105: 306–16.

[56] Llorca J, Domínguez M, Ledesma C, Chimentão RJ, Medina F, Sueiras J, Angurell I, Seco M, Rossell O. Propene epoxidation over TiO_2-supported Au–Cu alloy catalysts prepared from thiol-capped nanoparticles. J Catal 2008; 258: 187–98.

[57] Liu X, Wang A, Yang X, Zhang T, Mou CY, Suand DS, Li J. Synthesis of thermally stable and highly active bimetallic Au–Ag nanoparticles on inert supports. Chem Mater 2009; 21: 410–8.